Solar RRL

RESEARCH ARTICLE OPEN ACCESS

Gas Quenching-Mediated Crystallization for Optoelectronic-Grade Pb–Sn Perovskite Films

Yekitwork Abebe Temitmie[1,2] | Maria Azhar[1] | Muhammad Irfan Haider[1] | Yenal Yalcinkaya[1] | Emilia R. Schütz[1] | Tim Mayer[1] | Amare Benor[2] | Lukas Schmidt-Mende[1]

[1]Department of Physics, University of Konstanz, Konstanz, Germany | [2]Department of Physics, Bahir Dar University, Bahir Dar, Ethiopia

Correspondence: Lukas Schmidt-Mende (lukas.schmidt-mende@uni-konstanz.de)

Received: 5 September 2025 | **Revised:** 21 November 2025 | **Accepted:** 1 December 2025

Keywords: anti-solvent | gas-quenching | perovksite solar cell | Sn-Pb based perovksites

ABSTRACT

The fabrication of narrow-bandgap (NBG) Pb–Sn perovskites, with bandgaps typically around 1.1–1.3 eV, is often challenging due to issues related to repeatability, stability, and rapid crystallization kinetics. While Sn–Pb perovskites offer advantages such as defect tolerance and lower toxicity, they are also prone to inhomogeneous crystallization. Sn-based component of perovskite crystallizes much faster than the Pb-based component, leading to poor film coverage, pinholes, and rough morphologies. In this study, we employed gas quenching (GQ) instead of the commonly used antisolvent (AS) quenching to address the rapid crystallization issue. GQ approach resulted in slower crystallization and improved film quality. Besides, GQ produced more reproducible results compared to AS quenching. Devices fabricated using the GQ method also demonstrated better performance with higher open-circuit voltage (V_{OC}) values. Specifically, devices prepared with the AS method achieved a power conversion efficiency (PCE) of 18.3%, whereas those using the GQ method reached a PCE of 19.1%. This improvement in efficiency combined with enhanced reproducibility, the simplicity, and environmental friendliness of the GQ approach underscores its advantage for processing NBG Pb–Sn mixed perovskite films. Therefore, the GQ method holds significant potential for application in the fabrication of NBG Pb–Sn perovskite solar cells.

1 | Introduction

The photovoltaic community has witnessed steady progress in perovskite solar cells (PSCs), driven by their outstanding performance. Power conversion efficiency (PCE) in lead-based PSCs has rapidly increased from an initial 3.8% reported in 2009 to a record 27.0% in 2025 [1–3]. Their cost-effectiveness [4], simple fabrication processes [5], and low-temperature processability [6] further highlight their significance and impact in the field of photovoltaics. Single-junction PSCs with higher efficiencies typically utilize lead-based perovskite materials [7–9]. However, despite their superior PCEs, PSCs face significant challenges, particularly regarding lead toxicity [10, 11]. In contrast, pure tin-based PSCs appear to overcome toxicity issues; however, their Sn^{2+} ions exhibit high reactivity and are prone to oxidation to Sn^{4+}, which severely compromises device stability. Additionally, pure tin-based perovskites tend to form defect-rich films with poor morphology and stability due to their high Lewis acidity and low activation energy, often resulting in uncontrolled nucleation, vacancy defects, and inferior film quality [12–14].

An alternative to lead-based PSCs is lead–tin (Pb–Sn) mixed perovskites, which offer the advantage of reduced toxicity compared to pure lead-based perovskites [15]. They also mitigate stability issues caused by the oxidation of Sn^{2+} to Sn^{4+}, which are more pronounced in pure tin-based perovskites [16, 17]. Additionally, Pb–Sn mixed perovskites exhibit a narrower bandgap (NBG) of approximately 1.1–1.3 eV; this narrowing is attributed to the bandgap bending effect relative to their pure counterparts [18–20]. Despite these significant advantages, Pb–Sn mixed NBG PSCs face persistent challenges, such as reproducibility issues [21–23]. These problems stem from faster crystallization, higher defect density, and sensitivity to moisture and oxygen [24]. The crystallization behavior of Sn–Pb mixed perovskite films is

crucial for device performance. To understand this issue, it is important to consider the underlying chemistry. Lanthanide contraction, which results in smaller atomic radii, typically leads to slower oxidation. Tin (Sn) does not experience lanthanide contraction, making it more prone to oxidation and consequently accelerating the crystallization of Sn-containing perovskite films [25]. To address the rapid crystallization issue, various strategies have been explored. For example, Yang et al. demonstrated that the desorption barrier of dimethyl sulfoxide (DMSO) is significantly higher for Sn-based complexes than for Pb-based ones, leading to asynchronous crystallization. By tailoring the solvent composition, particularly the DMSO content, they achieved synchronized Sn–Pb crystallization and homogeneous film formation [26]. In another study, Cheng Li et al. introduced N-hydroxythiophene-2-carboximidamide (NHC), a multifunctional additive, to control crystallization in tin-based PSCs [27]. Omar E. Solis et al. investigated the incorporation of thiophene-2-ethylammonium halides (TEAX) as additives in tin-based perovskite formulations, significantly enhancing film quality by effectively reducing Sn^{4+} formation and modulating crystallization dynamics [28]. Moreover, iso-pentylammonium tetrafluoroborate ($[PNA]BF_4$) was employed to selectively anchor Pb^{2+} ions, effectively modulating the crystallization process and resulting in a uniform distribution of Sn and Pb within the perovskite film [14]. While additives can control crystallization, they may also destabilize the crystal structure and cause bandgap fluctuations. Therefore, a mechanistic approach is necessary to precisely control the crystallization rate in Sn–Pb-based perovskites.

To address this issue in Pb–Sn NBG PSCs, we employed the gas quenching (GQ) method instead of the traditional antisolvent (AS) technique. GQ has emerged as a more environmentally friendly quenching process [29, 30]. Moreover, it eliminates the need for harmful chemicals, offers higher repeatability, and is industrially viable [22, 31, 32]. The GQ method works by gradually drying the perovskite material through exposure to an inert gas, such as nitrogen [33]. This controlled crystallization of perovskite films is crucial for producing high-quality films with fewer defects [34, 35]. Although researchers have demonstrated the applicability of GQ for perovskite film formation already, a detailed in situ transmission measurement to directly track rate of crystallization and its effect on grain sizes and how that contributes to overall performance of devices is still required. Our work resulted in significant improvements in device performance, with the PCE increasing from 18.3% for AS-processed devices to 19.1% for GQ-processed devices. Additionally, GQ enhances device repeatability by allowing a wider processing parameter window. We carefully investigated and compared AS- and GQ-processed films and devices using photoluminescence quantum yield (PLQY) measurements, atomic force microscopy (AFM), and grain size analysis. Furthermore, in situ transmittance measurements were used to analyze the effect of GQ on the rate of crystallization, grain sizes, and ultimately the overall device performance.

2 | Experimental Section

2.1 | Lead–Tin Perovskite Precursor Preparation

The NBG Pb–Sn mixed perovskite with the composition $(FASnI_3)_{0.6}(MAPbI_3)_{0.4}$ was synthesized by combining $FASnI_3$ and $MAPbI_3$ solutions. For the 1.15 M $FASnI_3$ solution, 18 mg of SnF_2 (10 mol%), 197.8 mg of FAI, and 428.4 mg of SnI_2 were dissolved in 1 mL of solvent (800 μL DMF and 200 μL DMSO) and stirred overnight at room temperature. For the 1.15 M $MAPbI_3$ solution, 530 mg of PbI_2, 183 mg of MAI, and 3.5 mol% $Pb(SCN)_2$ additive were dissolved in 0.7 mL of solvent (630 μL DMF and 70 μL DMSO). The mixture was stirred for 30 min at 70°C and then stirred again overnight at room temperature. Subsequently, the $FASnI_3$ precursor solution was filtered through a 0.2 μm PTFE filter, and then the two precursors were mixed in a 3:2 $FASnI_3$:$MAPbI_3$ ratio. The resulting Sn–Pb mixed precursor solution was stirred at room temperature for 30 min before use.

2.2 | Hole Transport Layer Precursors Deposition

The ITO substrates were sequentially cleaned for 30 min using detergent, deionized water, acetone, and isopropyl alcohol (IPA) under ultrasonication. After drying with nitrogen gas, the substrates were treated with UV–ozone for 20 min. A 0.5 mM self-assembled monolayer (SAM) film was deposited on the cleaned ITO substrates using a two-step method. First, the substrate was held stationary for 20 s after the SAM solution was applied, followed by spinning at 3000 rpm for 30 s inside the glovebox, and then annealed at 100°C for 10 min. After SAM deposition, the substrates were transferred outside the glovebox for PEDOT:PSS deposition. The PEDOT:PSS dispersion was filtered through a 0.45 μm PVDF filter before use and then spin coated onto the SAM-coated ITO at 8000 rpm for 40 s and subsequently annealed at 120°C for 20 min, as shown in Figure S2.

2.3 | Lead–Tin Perovskite Film Fabrication

2.3.1 | Film Preparation Using Antisolvent Quenching

The perovskite precursor solution (30 μL) was statically deposited and spin coated onto the hole transport layers (HTLs) at 4000 rpm for 60 s. Diethyl ether (700 μL) was used as the AS and was dripped onto the film 15 s after the start of the spin-coating process. All perovskite films were then annealed at 100°C for 10 min.

2.3.2 | Perovskite Film Preparation Using Gas Quenching

A 30 μL of perovskite precursor solution was statically deposited and spin coated onto the HTLs at 4000 rpm for 60 s. Nitrogen gas was employed to induce perovskite crystallization. Among various pressures tested, the optimal results were achieved using a circular nozzle nitrogen gun with a diameter of 1 mm and a regulator pressure of approximately 5 bar, as shown in Figure 2 as compared to Figure S4. The nitrogen gun was positioned perpendicularly, 5 cm above the spinning substrate. After 15 s of spinning the precursor solution, the substrates were subjected to nitrogen gas blowing for 20 s, followed by an additional 25 s of spinning. All perovskite films were subsequently annealed at 100°C for 10 min.

2.4 | Lead–Tin Perovskite Solar Cells Fabrication

Following the procedures outlined in Section 2.3, AS and GQ processes started with spin coating of perovskite precursor solution. The next processes in preparing the device, such as thermally evaporating the electron transport layers and metal electrodes (vacuum $< 6 \times 10^{-6}$ mbar) to complete the device fabrication, were done identically for all cells. This made sure that the device design was the same (see Figure 1). Finally, 25 nm of C_{60} with the deposition rate of 0.3 Å/s, 7 nm of BCP with the rate of 0.2 Å/s, and 100 nm of Ag with the deposition rate of 1.0 Å/s were sequentially evaporated on the top of perovskite. An optimized 70 nm thick MgF_2 layer was thermally evaporated on the glass side of PSCs (at a rate of 1 Å/s) as an antireflection coating.

The chemical structures of the ((2-(9H-carbazol-9-yl)ethyl)phosphonic acid) (2PACz) and Poly(3,4-ethylenedioxythiophene) polystyrene sulfonate (PEDOT:PSS) shown in Figure S1, which serve as HTL layers in the full Pb–Sn mixed PSC device architecture (ITO/SAM/PEDOT:PSS/perovskite/C_{60}/BCP/Ag), demonstrate the different quenching techniques, i.e., AS and GQ, as shown in Figure S2, providing insight into their molecular composition and potential influence on film formation and charge transport.

2.5 | Characterization

2.5.1 | Film Characterization

The work function of perovskite film deposited on SAM/PEDOT:PSS was characterized using photoelectron spectroscopy in air (PESA) conducted on an AC-2 system (Riken Instruments), enabling us to understand the impact of the quenching process of perovskite on energy level alignment. To compare the optoelectronic quality of perovskite films prepared via AS and GQ methods, we measured the PLQY (PLQY, LuQY Pro system, Quantum Yield Berlin). Besides, surface morphology and microstructural features property of perovskite film were studied by AFM (Park NX-10 AFM) and scanning electron microscopy (SEM, Gemini 500 FESEM system Zeiss). Furthermore, in situ transmission measurements were performed during the spin-coating process to monitor the film formation dynamics under the two different quenching approaches.

2.5.2 | Device Characterization

Current density–voltage (J–V) characteristics of the PSCs were recorded under 1 Sun (1 kW/m^2) illumination in a nitrogen-filled glovebox using a Keithley 2400 SMU and LOT 300W Xenon solar simulator, calibrated with a Fraunhofer ISE-certified silicon reference diode equipped with a KG5 filter window. Measurements were carried out with a voltage step size of 0.02 V and a delay of 0.01 s. Maximum power point (MPP) tracking and open-circuit voltage (V_{OC}) rise and decay analysis were employed to ensure reliable PSC evaluation. Both light and dark J–V curves of the champion device were obtained.

3 | Results and Discussion

3.1 | Perovskite Solar Cells Device Analysis

Hereafter, AS films/devices refer to those in which perovskite quenching was performed using the AS method, whereas GQ films/devices refer to those in which perovskite quenching was performed using the GQ method. Figure 2 presents a box plot of the photovoltaic performance of AS and GQ devices, showing open-circuit voltage (V_{OC}), short-circuit current density

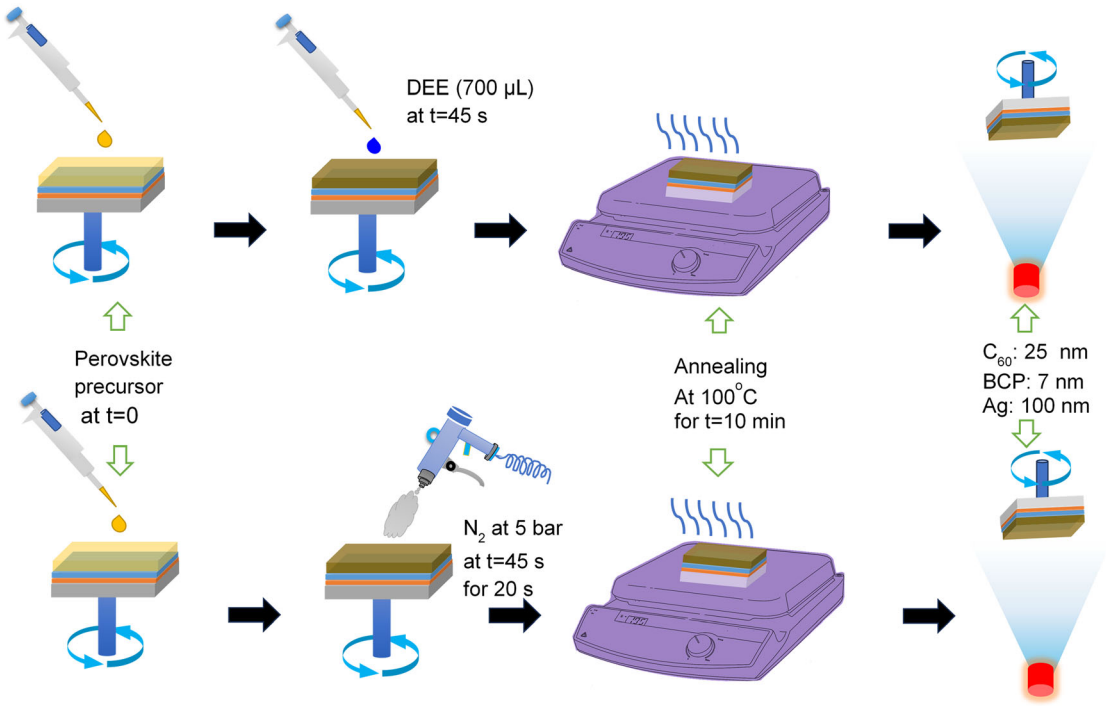

FIGURE 1 | Schematic representation of device fabrication, illustrating the process from perovskite layer deposition to thermal evaporation of precursors, with emphasis on AS and GQ techniques. AS = antisolvent; GQ = gas quenching.

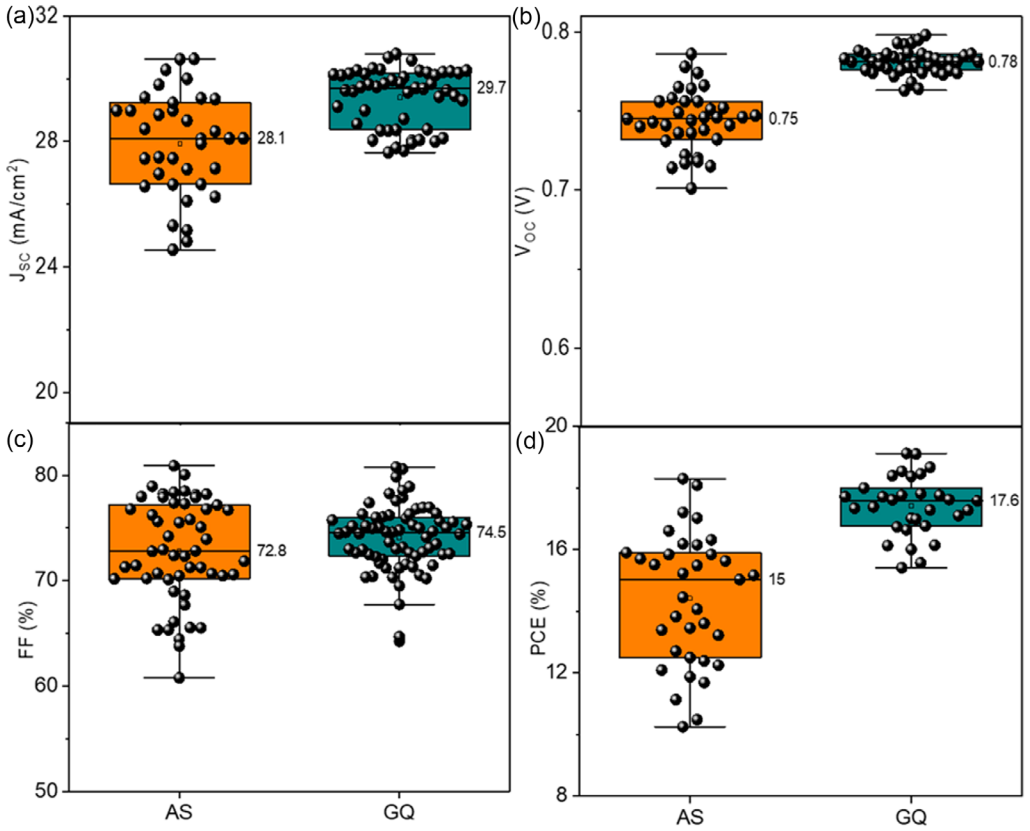

FIGURE 2 | Boxplots of the photovoltaic parameters of Pb–Sn mixed PSCs fabricated using AS (left, orange) and GQ (right, green) at a gas pressure of 5 bar. The parameters shown are current density (J_{sc}), open-circuit voltage (V_{oc}), FF, and PCE in panels (a–d), respectively. AS = antisolvent; FF = fill factor; GS = gas quenching; PSC = perovskite solar cells; PCE = power conversion efficiency.

(J_{SC}), fill factor (FF), and overall PCE. The GQ devices demonstrate a higher V_{OC}, suggesting a reduced defect density, as supported by the higher PLQY values for GQ devices (see Section 3.2). The FF results appear comparable; however, notably, the data for all parameters, including FF, J_{SC}, $V_{OC,}$ and overall PCE, are consistent, showing only slight deviations from the average values for GQ devices. The reproducibility of the GQ method is further demonstrated by the narrow distribution of all photovoltaic parameters in the box plot, which also indicates relatively higher average values for each parameter, highlighting the superior performance of the GQ method.

As a result, the gas-quenched device exhibits a higher V_{OC} of 0.79 V, contributing to its PCE of 19.1%. In comparison, the AS-treated counterpart has a lower V_{OC} of 0.77 V, leading to a reduced PCE of 18.3%. A comprehensive comparison of the photovoltaic parameters for PSCs processed via both AS and GQ methods is presented in Table S1. This table summarizes the average and champion values for key device metrics, enabling a clear evaluation of the impact of each processing technique on device performance.

To further investigate the reasons behind the differing performance of AS and GQ devices, V_{OC} rise and decay measurements were conducted under varying illumination conditions (light on/off) at intervals ranging from 0 to 70 s, in 10 s increments. Figure 3a compares the V_{OC} rise and decay behavior of PSCs prepared using the AS and GQ methods. The V_{OC} response differs notably between the two methods, particularly in the speed of rises upon illumination and the rate of decay after the light is turned off. The GQ devices exhibit a more pronounced and rapid V_{OC} rise, reaching a maximum value of 0.80 V shortly after illumination begins. In contrast, the AS devices show a slower V_{OC} rise, reaching only 0.77 V. During the decay phase, the GQ cells display a sharper decline, with the voltage dropping to 0 V, indicating rapid carrier recombination and minimal trap-assisted retention. Conversely, AS-treated films demonstrate a slower V_{OC} decay, with residual voltage persisting after illumination ceases. This lingering signal suggests the presence of trap states or grain boundary defects that impede carrier recombination and may contribute to increased hysteresis (Figure 3d) and reduced device efficiency (see Figure 2).

The MPP tracking measurements shown in Figure 3b were conducted inside a nitrogen-filled glovebox without encapsulation, under continuous illumination for 90 s. The steady-state PCEs of the AS and GQ devices are 18.0% and 18.5%, respectively. However, the AS devices exhibit more rapid decline in power output. This is likely due to suboptimal film morphology and inherent instabilities that can occur even in an inert glovebox environment, such as residual solvent effects, incomplete crystallization, or interfacial defects formed during processing.

Moreover, the GQ device exhibits a significantly lower dark current compared to the AS devices, with a current density of 1.98×10^{-5} mA/cm^2 at 0.0 V, indicating reduced leakage. In contrast, the AS device shows a higher dark current density of 1.96×10^{-4} mA/cm^2 as illustrated in Figure 3c. These results confirm that controlled crystallization via the GQ method leads to improved diode quality and reduced nonradiative losses in the

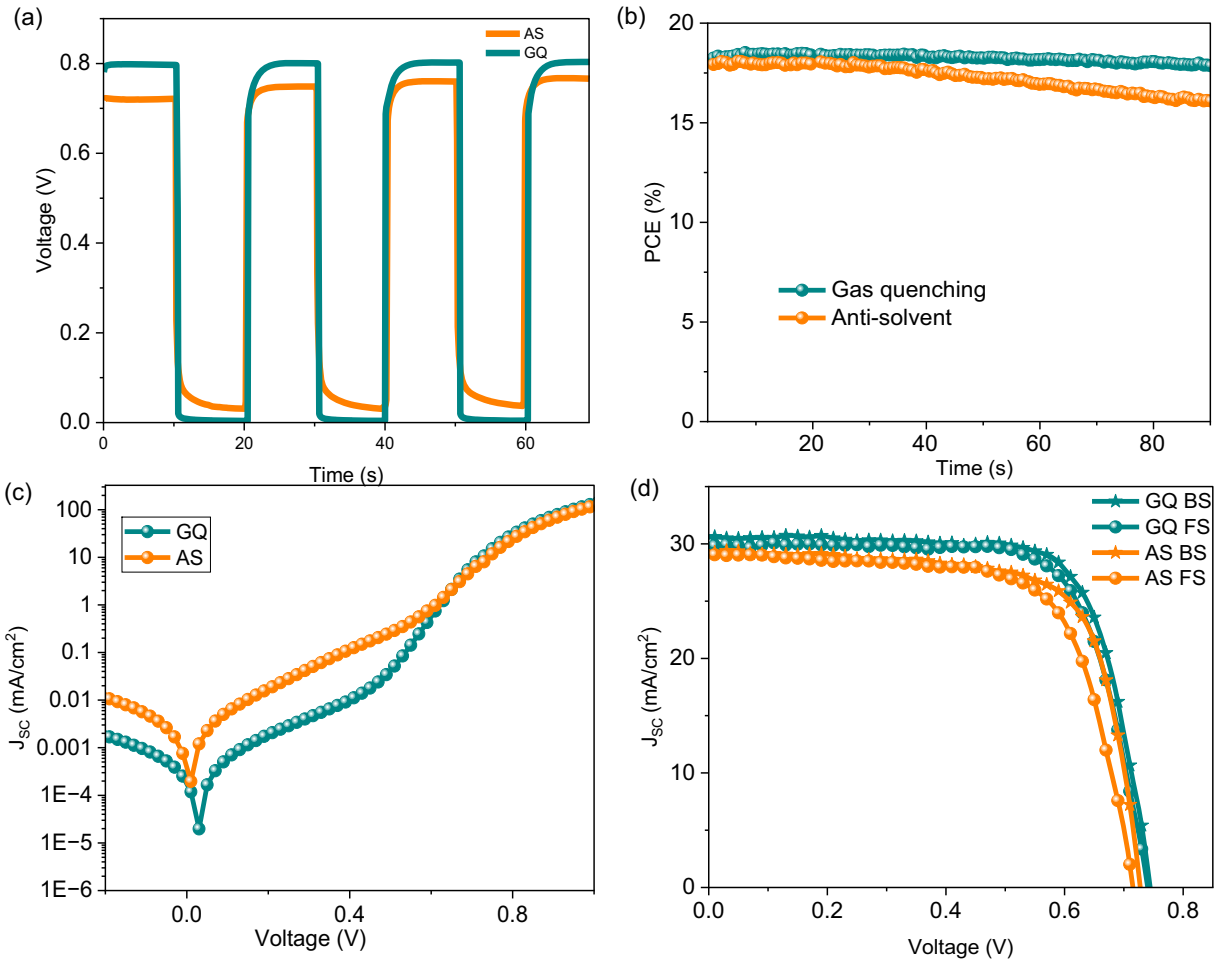

FIGURE 3 | (a) V_{OC} decay and rise measurements of the best-performing cells in both scenarios, (b) MPP tracking of PSCs for 90 s following the initial measurement inside the glovebox, (c) dark and (d) light *J–V* curves of devices fabricated via GQ and AS methods under FS and BS scans. AS = antisolvent; BS = backward scan; FS = forward scan; GQ = gas quenching; MPP = maximum power point; PSC = perovskite solar cell.

device. In Figure 3d, the light *J–V* curves for both GQ and AS devices were measured in both FS (0 V to V_{OC}) and BS (V_{OC} to 0 V) directions to assess the presence of hysteresis. For the GQ device, the FS and BS nearly perfectly overlap, indicating minimal hysteresis, with a hysteresis index of 0.0021 compared to 0.0182 for the AS device; both values were calculated from current density measurements. This minimal hysteresis suggests that the GQ film has a uniform morphology, efficient charge transport, and reduced ion migration, all of which contribute to repeatable, improved, and more stable device performance. To confirm that the improved performance is indeed correlated with enhanced film quality, we performed additional measurements.

3.2 | Perovskite Film Analysis

An important tool for assessing perovskite film quality is the PLQY. Therefore, we conducted a comparative analysis of PLQY and quasi-Fermi-level splitting (QFLS) for perovskite films deposited on ITO/SAM/PEDOT substrates using the AS and GQ methods. This analysis provided valuable insights into film quality and recombination losses in the solar cells. PLQY measurements were performed under varying illumination intensities, ranging from 0.1 to 1 sun in increments of 0.2 sun. The GQ films exhibited a higher PLQY value of 0.28%, with an average of 0.19%, compared to 0.21% and an average of 0.12% for the AS films, as shown in Figure 4a. This indicates more efficient radiative recombination and reduced nonradiative losses in the GQ-processed films. Similarly, Figure 4b shows the QFLS values, where the GQ films exhibit a higher QFLS of 0.85 V compared to 0.81 V for the AS films. The higher QFLS suggests that the GQ method produces better-quality perovskite films with the fewer defect states that lower the QFLS. Moreover, since QFLS directly indicates the maximum achievable V_{OC} and reflects the extent of nonradiative losses, the higher QFLS in GQ-processed films implies superior electronic quality and a greater capacity to support photovoltage under illumination. This enhancement likely results from both improved bulk properties and superior interface quality, as the GQ method may promote better contact between the perovskite layer and adjacent charge transport layers, further suppressing interfacial recombination [36].

In addition to PLQY measurements, AFM is an essential characterization technique for examining the surface topography and roughness of materials at the nanoscale. It offers valuable insights into the surface properties of perovskite films, as shown in Figure 4c(AS), 4d(GQ).

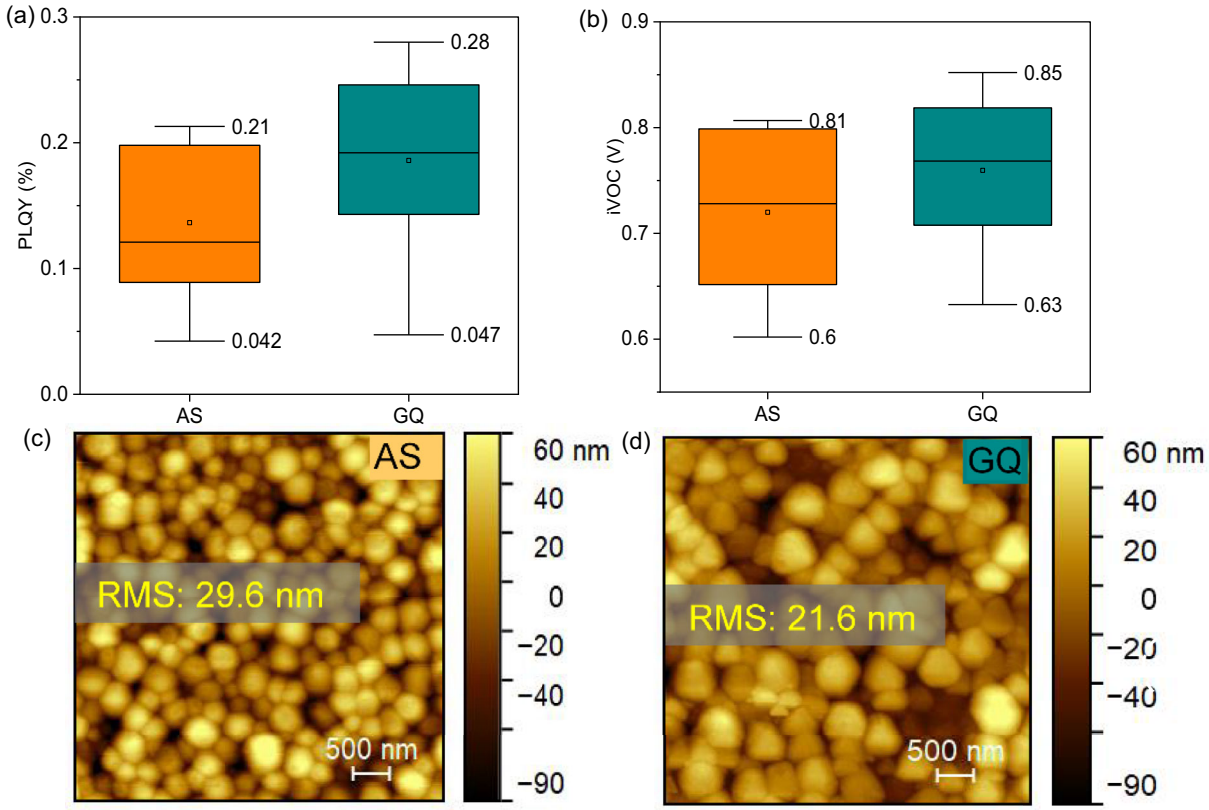

FIGURE 4 | (a) The PLQY and the (b) QFLS. AFM topography images with RMS surface roughness of the perovskite film, under (c) AS and (d) GQ method of the perovskite films. AS = antisolvent; AFM = atomic force microscope; GQ = gas quenching; PLQY = photoluminescence quantum yield; QFLS = quasi-Fermi-level splitting.

The film-forming properties of perovskite significantly influence the performance of PSC devices. The morphologies of perovskite layers prepared by the AS and GQ methods were examined using AFM. In both cases, topographic AFM images were obtained for perovskite films deposited on ITO/SAM/PEDOT:PSS substrates. The root mean square (RMS) roughness of the perovskite layer formed via the AS method is 29.6 nm, whereas the GQ-processed film exhibits a reduced RMS roughness of 21.6 nm. The AS film displays a less uniform surface compared to the GQ film. In contrast, the GQ perovskite film shows a smoother and more uniform topography, which is advantageous for the deposition of subsequent layers. Table S2 in the supporting information (SI) provides RMS and peak-to-valley roughness values corresponding to the AFM surface profiles of perovskite films prepared using the AS and GQ techniques.

In the next step, we investigated the crystallization process in greater detail to understand its role on film morphology. For this purpose, we employed in situ transmission measurements (detailed setup provided in the SI) as shown in Figure 5a,b. These measurements provide valuable insights into the crystallization dynamics of perovskite films processed via the AS and GQ methods, respectively. In the AS method, the AS is dripped onto the spinning substrate within a fraction of a second, whereas in the GQ method, perovskite films undergo continuous drying under a directed nitrogen gas flow for 20 s. These differences in quenching type and duration affect the overall quenching rate. To investigate this effect, an in situ transmittance setup was used to study how the quenching rate influences perovskite film crystallization. In both cases, in situ transmittance measurements were conducted for 60 s, with the respective treatments applied at 15 s. Prior to this point, the perovskite precursor film remains in a liquid, transparent state, resulting in high transmittance due to minimal light absorption. Upon dripping the AS after 15 s, a rapid and sharp decrease in transmittance over approximately 5 s was observed, indicating a fast crystallization rate. This is attributed to the rapid extraction of coordinating solvents (DMF and DMSO) by the AS (diethyl ether, DEE), which induces fast nucleation and crystallization of the perovskite phase. In contrast, GQ films show no significant change in transmittance during the first 5 s after quenching. After approximately 10 s, a clear change in the transmission spectrum occurs, followed by another 10–15 s of gradual transmission shift. After 40 s, the transmission spectra of both films are very similar. These results suggest a comparatively slower crystallization rate for GQ samples. However, the perovskite films produced using the AS and GQ methods have ionization potentials of 5.47 and 5.44 eV, respectively. Both processing techniques yield films with relatively similar HOMO values, exhibiting only a slight shift in energy levels, as indicated by the small difference between the two values (see Figure S5).

Rapid crystallization is often induced by AS quenching, which can lead to uncontrolled nucleation. This results in smaller grain sizes and increased defect density, negatively impacting charge transport and recombination [37]. As established in the literature [38], slower crystallization reduces nucleation density and allows extended grain growth, resulting in larger crystal domains. To clarify this mechanism, we have included a schematic (Figure 5c) contrasting AS quenching and GQ. In the AS case, rapid supersaturation produces many nuclei that limit

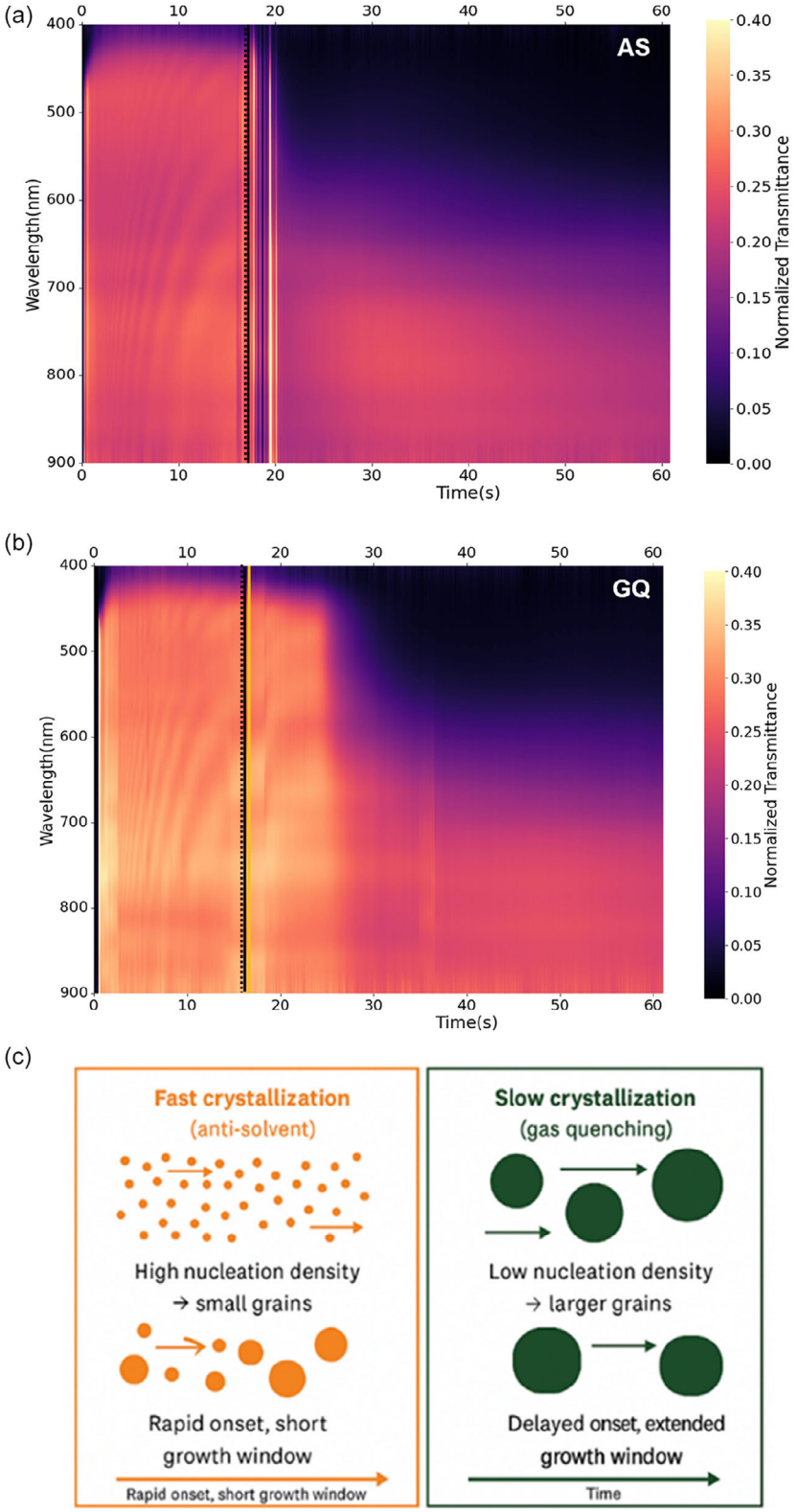

FIGURE 5 | In situ transmission spectra of the perovskite film during the spin-coating and quenching processes for the (a) AS and the (b) GQ method. In both cases, quenching begins at approximately $t = 15$ s. (c) Schematic illustration of nucleation and growth dynamics under fast (AS) and slow (GQ) crystallization. AS = antisolvent; GQ = gas quenching.

grain size, whereas in the GQ case, nucleation occurs more gradually, enabling grains to grow larger before impingement. This schematic explanation is consistent with our SEM observations.

The slower crystallization process results in different grain sizes, as shown by SEM analysis. Figure 6 provides a detailed comparison of the grain morphology of perovskite films deposited on PEDOT:PSS, which is coated on SAM-treated ITO substrates,

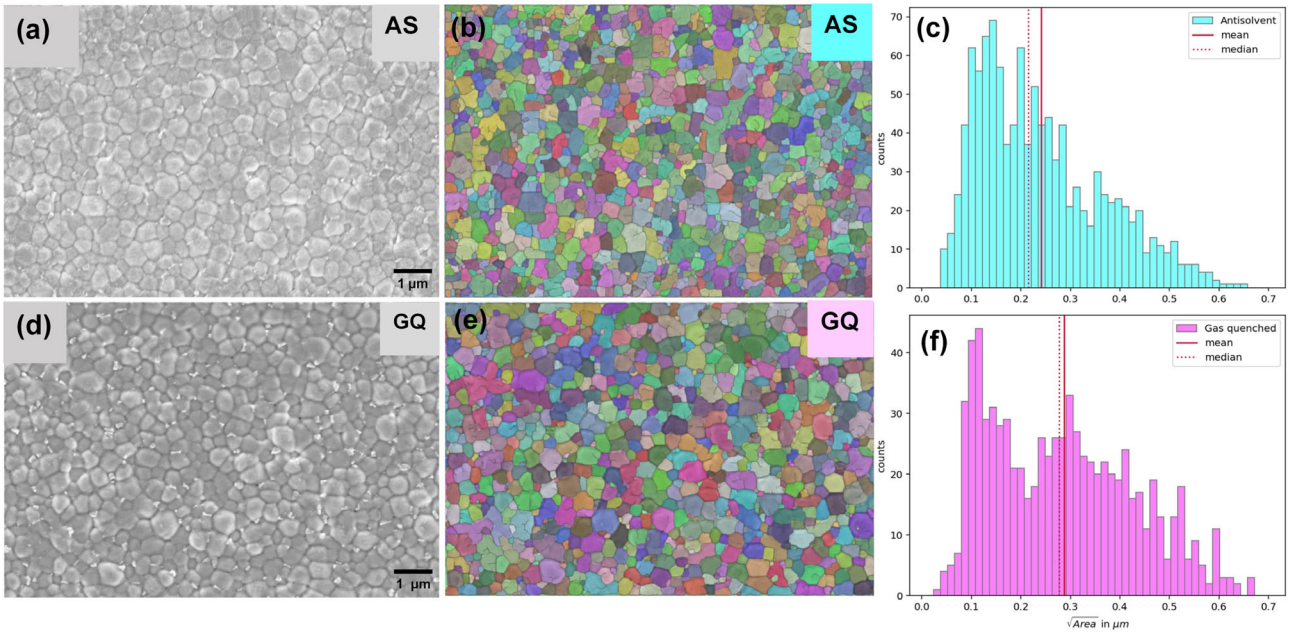

FIGURE 6 | SEM image of perovskite film at 10,000x magnification under (a) AS and (d) GQ methods. (b) and (e) The color scheme grain-identified perovskites for the two techniques. Histogram of grain distribution of perovskite films induced by (c) AS and (f) GQ. AS = antisolvent; GQ = gas quenching.

under both AS and GQ processing conditions. The SEM images in Figure 6a(AS), d(GQ) were used for grain size extraction, while Figure 6b,e highlights the identified grains through color segmentation. The corresponding histograms in Figure 6c,f, depicting grain size distribution, reveal a slight difference between the two films: the AS films exhibit a mean grain size of approximately 0.25 μm, whereas the GQ films show a larger mean grain size of about 0.3 μm. Although the width of the grain size distributions is much greater than the difference observed between the GQ and AS samples, other distinct differences are evident in the histograms. A side peak appears for smaller grain sizes in the GQ film (Figure 6f), representing smaller structures that form at the grain boundaries and appear as light spots in Figure 6d. The presence of these structures in the histogram shifts the mean and median values toward lower values for the GQ sample. Therefore, the actual difference in grain sizes between the GQ and AS samples is likely larger than indicated here. This slight increase in grain size for the GQ method could be attributed to a slower crystallization rate, which promotes slower film formation and consequently larger grains. Larger grains are known to reduce grain boundary density, thereby enhancing charge transport and reducing nonradiative recombination losses. This finding demonstrates a clear correlation among the SEM grain size analysis, PLQY measurements, and AFM topography results presented in this study.

4 | Repeatability of GQ Devices

As discussed earlier and demonstrated by the graphs in Figure 2, GQ devices demonstrate higher repeatability compared to AS devices. The GQ devices exhibit a narrower distribution of solar cell efficiencies, ranging from 15.4% to 19.1% ($\Delta = 3.7\%$), whereas the AS method produces a comparatively wider range, from 10.3% to 18.3% ($\Delta = 8.0\%$). This 4.3% reduction in spread indicates that the GQ method yields devices that are more consistent and repeatable. This suggests that GQ is less sensitive to exact processing parameters. As also reported by Samantha C. Kaczaral et al., the repeatability of perovskite film formation appears to be enhanced using the GQ method, potentially due to the slower and more controlled crystallization dynamics achieved by this approach [23]. The timing of perovskite film formation is crucial to ensure that the final film is of high quality and reproducible. As shown in Figure 5, in situ spectral measurements reveal that the AS method induces rapid nucleation, resulting in a narrower processing window, increased sensitivity to timing variations, and consequently less repeatability. In

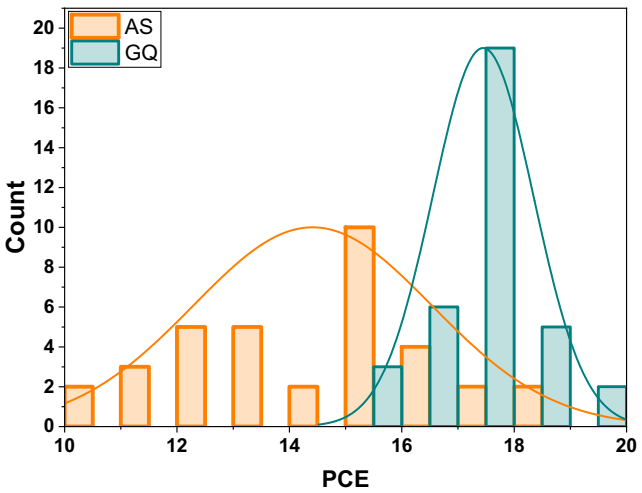

FIGURE 7 | A comparative statistical distribution of PCE for AS and GQ devices, presenting the mean values and standard deviations to illustrate the consistency and variability of performance across samples. AS = antisolvent; GQ = gas quenching; PCE = power conversion efficiency.

contrast, the GQ method slows and regulates the crystallization process, leading to more uniform spectral evolution and improved reproducibility across devices. This is confirmed by the performance parameters shown in Figure 2, where GQ devices exhibit a higher mean PCE of 17.6% with a standard deviation of 0.9%, compared to AS devices, which show a lower mean efficiency of 15% and a higher standard deviation of 2.1% (Figure 7).

5 | Conclusion

We conducted a step-by-step comparison of AS and GQ devices for our Sn-Pb-based NBG perovskite. Devices fabricated using GQ exhibited a minimal hysteresis index of 0.002 in light *J–V* scans and superior diode characteristics in dark *J–V* analysis, indicating reduced defect-mediated recombination. In contrast, AS films showed a pronounced hysteresis index of 0.018. Furthermore, GQ devices demonstrated a higher champion PCE of 19.1%, compared to 18.3% for AS devices. Additionally, we observed a slower crystallization rate in perovskites processed with GQ, as evidenced by in situ measurements. SEM grain analysis revealed that, due to the slower crystallization rate in GQ films, the perovskite grain size was comparatively larger than in AS films. PLQY measurements indicated a higher PLQY for GQ films, suggesting a reduced defect density. AFM analysis showed that GQ films were smoother than AS films. These results underscore the effectiveness of the GQ method as a strategy for producing high-performance PSCs. GQ, in particular, has demonstrated promise in enhancing repeatability and device performance in Pb–Sn mixed perovskites, a factor that is very important in the industrial production of such cells. Additionally, GQ offers a more sustainable processing method without the use of solvents. Although this study focuses on Sn–Pb-based films, other results from our group demonstrate that the performance of GQ-processed films also improves for other perovskite compositions. Therefore, GQ appears to be the generally preferred method over AS treatment because it offers not only a more sustainable and less toxic preparation process, but also a slower crystallization rate, improved film quality, enhanced repeatability, more stable device performance, and superior photovoltaic efficiency.

Acknowledgments

Y.A.T. gratefully acknowledges funding from the Deutsche Forschungsgemeinschaft (DFG). M.A. is funded by the Deutscher Akademischer Austauschdienst (DAAD) through a research grant for doctoral programs in Germany, funding number 57645448. M.I.H. acknowledges funding from the German Federal Ministry for Economic Affairs and Climate Action (BMWK) through the APERO project (reference number 03EE1113C). Y.Y. was funded by the DFG (project number 533867117).

Open Access funding enabled and organized by Projekt DEAL.

Funding

This study was supported by the Deutsche Forschungsgemeinschaft (ID0EGFBG33281), German Academic Exchange Service New Delhi (57645448), BMWK (03EE1113C), Deutsche Forschungsgemeinschaft (DFG)(DE).

Conflicts of Interest

The authors declare no conflicts of interest.

Data Availability Statement

The data that support the findings of this study are available from the corresponding author upon reasonable request.

References

1. A. Kojima, K. Teshima, Y. Shirai, and T. Miyasaka, "Organometal Halide Perovskites as Visible-Light Sensitizers for Photovoltaic Cells," *Journal of the American Chemical Society* 131, no. 17 (2009): 6050–6051.

2. NREL, "*Best Research-Cell Efficiencies*," accessed January 2025, https://www.nrel.gov/pv/cell-efficiency.html.

3. G. Yan, Y. Yuan, M. Kaba, and T. Kirchartz, "Visualizing Performances Losses of Perovskite Solar Cells and Modules: From Laboratory to Industrial Scales," *Advanced Energy Materials* 15, no. 3 (2025): 2403706.

4. Q. Zhou, X. Liu, Z. Liu, et al., "Annual Research Review of Perovskite Solar Cells in 2023," *Materials Futures* 3 (2024): 2752–5724.

5. R. A. Afre and D. Pugliese, "Perovskite Solar Cells: A Review of the Latest Advances in Materials, Fabrication Techniques," *And Stability Enhancement Strategies. Micromachines* 15, no. 2 (2024): 192.

6. S. Wu, C. Li, S. Y. Lien, and P. Gao, "Temperature Matters: Enhancing Performance and Stability of Perovskite Solar Cells through Advanced Annealing Methods," *Chemistry* 6, no. 1 (2024): 207–236.

7. J. Jeong, M. Kim, J. Seo, et al., "Pseudo-Halide Anion Engineering for α-FAPbI3 Perovskite Solar Cells," *Nature* 592, no. 7854 (2021): 381–385.

8. S. Tao, I. Schmidt, G. Brocks, et al., "Absolute Energy Level Positions in Tin-and Lead-Based Halide Perovskites," *Nature Communications* 10, no. 1 (2019): 2560.

9. S. Li, Y. Jiang, J. Xu, et al., "High-Efficiency and Thermally Stable FACsPbI3 Perovskite Photovoltaics," *Nature* 635, no. 8037 (2024): 82–88.

10. Y. Yin, L. Yang, X. Zhang, and J. Zhang, "Pernicious Effects and Management of Lead Leakage from Perovskite Solar Cells," *Journal of Materials Chemistry A* 11, no. 47 (2023): 25825–25848.

11. P. T. Mokabane, V. T. Lukong, and T. C. Jen, "A Review of the Effect of Stability Issues and Wide-Bandgap in the Application of Perovskite Solar Cells," *Materials for Renewable and Sustainable Energy* 14, no. 2 (2025): 34.

12. F. Hao, C. C. Stoumpos, P. Guo, et al., "Solvent-Mediated Crystallization of CH3NH3SnI3 Films for Heterojunction Depleted Perovskite Solar Cells," *Journal of the American Chemical Society* 137, no. 35 (2015): 11445–11452.

13. H. Dong, C. Ran, W. Gao, et al., "Crystallization Dynamics of Sn-Based Perovskite Thin Films: Toward Efficient and Stable Photovoltaic Devices," *Advanced Energy Materials* 12, no. 1 (2022): 2102213.

14. Z. Zhang, J. Liang, Y. Zheng, et al., "Balancing Crystallization Rate in a Mixed Sn–Pb Perovskite Film for Efficient and Stable Perovskite Solar Cells of More than 20% Efficiency," *Journal of Materials Chemistry A* 9, no. 33 (2021): 17830–17840.

15. L. Xiao, T. An, C. Deng, X. Xu, and H. Sun, "On Biosafety of Sn-Containing Halide Perovskites," *Energy & Environmental Science* 16, no. 5 (2023): 2120–2132.

16. L. Lanzetta, T. Webb, N. Zibouche, et al., "Degradation Mechanism of Hybrid Tin-Based Perovskite Solar Cells and the Critical Role of Tin (IV) Iodide," *Nature Communications* 12, no. 1 (2021): 2853.

17. J. P. Correa-Baena, M. Saliba, T. Buonassisi, et al., "Promises and Challenges of Perovskite Solar Cells," *Science* 358, no. 6364 (2017): 739–744.

18. H. Lee, S. B. Kang, S. Lee, K. Zhu, and D. H. Kim, "Progress and Outlook of Sn–Pb Mixed Perovskite Solar Cells," *Nano Convergence* 10, no. 1 (2023): 27.

19. A. Goyal, S. McKechnie, D. Pashov, W. Tumas, M. Van Schilfgaarde, and V. Stevanovic, "Origin of Pronounced Nonlinear Band Gap Behavior in Lead–tin Hybrid Perovskite Alloys," *Chemistry of Materials* 30, no. 11 (2018): 3920–3928.

20. J. Im, C. C. Stoumpos, H. Jin, A. J. Freeman, and M. G. Kanatzidis, "Antagonism between Spin–orbit Coupling and Steric Effects Causes Anomalous Band Gap Evolution in the Perovskite Photovoltaic Materials CH3NH3Sn1–x Pb x I3," *The Journal of Physical Chemistry Letters* 6, no. 17 (2015): 3503–3509.

21. M. D. Farrar, In Improving the Performance and Reproducibility of Lead-Tin Perovskite Absorbers toward All Perovskite Tandem Solar Cells (Doctoral dissertation, University of Oxford, 2022).

22. Y. Yu, F. Zhang, T. Hou, X. Sun, H. Yu, and M. Zhang, "A Review on Gas-Quenching Technique for Efficient Perovskite Solar Cells," *Solar RRL* 5, no. 10 (2021): 2100386.

23. S. C. Kaczaral, D. A. Morales, S. W. Schreiber, et al., "Improved Reproducibility of Metal Halide Perovskite Solar Cells via Automated Gas Quenching," *APL Energy* 1, no. 3 (2023): 036112.

24. T. Li, F. Ma, Y. Hao, et al., "Defect Passivation for Highly Efficient and Stable Sn-Pb Perovskite Solar Cells," *Crystals* 14, no. 9 (2024): 802.

25. M. M. Byranvand, W. Zuo, R. Imani, M. Pazoki, and M. Saliba, "Tin-Based Halide Perovskite Materials: Properties and Applications," *Chemical Science* 13, no. 23 (2022): 6766–6781.

26. X. Yang, T. Ma, H. Hu, et al., "Understanding and Manipulating the Crystallization of Sn–Pb Perovskites for Efficient All-Perovskite Tandem Solar Cells," *Nature Photonics* 19 (2025): 1–8.

27. C. Li, M. Zhu, H. Jiang, et al., "Multiple Active Site Additive-Mediated Suppression of Sn 2+ Oxidation and Regulation of Crystallization for High-Performance Sn–Pb Mixed Perovskite Solar Cells," *Materials Horizons* 12, no. 13 (2025): 4813–4821.

28. O. E. Solis, M. Mínguez-Avellán, P. F. Betancur, et al., "Adjusting the Crystallization of Tin Perovskites through Thiophene Additives for Improved Photovoltaic Stability," *ACS Energy Letters* 9, no. 11 (2024): 5288–5295.

29. J. Chen, J. Liu, Y. Li, et al., "Ultrasonic-Assisted Processing Combined with Gas Quenching for Fabricating High-Performance and Stable Inverted Perovskite Solar Cells," *Advanced Functional Materials* 34, no. 26 (2024): 2314652.

30. S. Tang, J. Bing, J. Zheng, et al., "Complementary Bulk and Surface Passivations for Highly Efficient Perovskite Solar Cells by Gas Quenching," *Cell Reports Physical Science* 2, no. 8 (2021): 100511.

31. A. Babayigit, J. D'Haen, H. G. Boyen, and B. Conings, "Gas Quenching for Perovskite Thin Film Deposition," *Joule* 2, no. 7 (2018): 1205–1209.

32. F. Yang, D. Jang, L. Dong, et al., "Upscaling Solution-Processed Perovskite Photovoltaics," *Advanced Energy Materials* 11, no. 42 (2021): 2101973.

33. M. Azhar, Y. Yalcinkaya, D. T. Cuzzupè, Y. Temitmie, M. I. Haider, and L. Schmidt-Mende, "Perovskite Thin Films Solar Cells: The Gas Quenching Method," *Materials and Sustainability* 1, no. 1 (2025): 5.

34. J. Werner, T. Moot, T. A. Gossett, et al., M.D. Improving Low-Bandgap Tin–lead Perovskite Solar Cells via Contact Engineering and Gas Quench Processing," *ACS Energy Letters* 5, no. 4 (2020): 1215–1223.

35. A. Hadipour, "Enhancing Gas-Quenching Method for Fabrication of Perovskite-Based Photovoltaics," *Kuwait Journal of Science* 52, no. 2 (2025): 100387.

36. E. Butler-Caddle, K. I. Jayawardena, A. Wijesekara, R. L. Milot, and J. Lloyd-Hughes, "Distinguishing Carrier Transport and Interfacial Recombination at Perovskite/Transport-Layer Interfaces Using Ultrafast Spectroscopy and Numerical Simulation," *Physical Review Applied* 22, no. 2 (2024): 024013.

37. M. Azhar, D. T. Cuzzupè, Y. Yalcinkaya, et al., "Impact of Antisolvent and Gas Quenching on Wrinkling in Cs0. 15FA0. 85Pb (I0. 6Br0. 4) 3 Perovskite Films," *ACS Applied Materials & Interfaces* 17, 42 (2025): 58501–58511.

38. C. Liu, Y. B. Cheng, and Z. Ge, "Understanding of Perovskite Crystal Growth and Film Formation in Scalable Deposition Processes," *Chemical Society Reviews* 49, no. 6 (2020): 1653–1687.

Supporting Information

Additional supporting information can be found online in the Supporting Information section. **Supporting Fig. S1:** Chemical structures of 2PACz and PEDOT:PSS. 2PACz is a functionalized organic molecule used to modify surface properties, while PEDOT:PSS is a conductive polymer blend commonly employed as a hole transport layer in optoelectronic devices. **Supporting Fig. S2:** (a) Deposition of self-assembled monolayer (SAM); (b) thermal annealing of SAM at 100°C for 10 min; (c) deposition of PEDOT:PSS layer over the SAM; (d) annealing of the PEDOT:PSS film at 120°C for 20 min. **Supporting Fig. S3:** Schematic of the full-stack perovskite solar cell architecture, illustrating the layered configuration from substrate to top electrode (ITO/SAM/PEDOT:PSS/perovskite/C60/BCP/Ag). **Supporting Fig. S4:** Box plots comparing the photovoltaic performance of devices fabricated via gas quenching at (a) 2 bar and (b) 3 bar pressure. Each plot represents the distribution of key performance metrics across multiple devices. **Supporting Fig. S5:** Work function analysis of perovskite films grown on SAM/PEDOT:PSS layers using photoelectron spectroscopy in air (PESA), comparing samples prepared via antisolvent (AS) and gas quenching (GQ) methods. **Supporting Table S1:** A comprehensive summary of the average and champion values of the photovoltaic parameters for perovskite solar cells. These cells were subjected to both AS methods and GQ techniques. Parameters include power conversion efficiency (PCE), open-circuit voltage (V_{OC}), short-circuit current density (J_{SC}), and fill factor (FF). **Supporting Table. S2:** Quantitative analysis of surface roughness parameters.